Microstructure, Particle Size, and Magnetic Property of Fe-6.5 wt.% Si Nanocrystalline Alloys Prepared by Mechanical Alloying

YANG SUN,[1] YIYUE CHEN,[1] CHUNYAO LAN,[1] YOU TAN,[1] LIN ZHANG,[1] BOWEN DONG,[2] and SONG LAN [1,3]

1.—Department of Materials Science and Engineering, Chongqing Jiaotong University, Chongqing 400074, China. 2.—Momentive Technologies, Strongsville, OH 44149, USA. 3.—e-mail: sl1988@cqjtu.edu.cn

Fe-6.5 wt.% Si nanocrystalline alloys with good magnetic softness were prepared by mechanical alloying at various milling times (0–12 h) via a high-energy ball mill. Elemental iron and silicon powders were used as raw materials. Structural evolution, particle size distribution, and magnetic properties were investigated for as-milled Fe-Si alloy powders. During the alloying process, Si atoms dissolve substitutionally into α-Fe lattice, causing a decrease of lattice parameter with the milling time. A single α-(Fe,Si) solid-solution phase with grain size of ~ 10 nm is obtained, and no ordered phases (B2 or DO3) are observed. Ball-milling effectively reduces particle size of the alloy powders from 64 μm to 30 μm, and exhibits a controlled distribution of the particle size. A transition in the dominant factor and a deviation from the sixth power law on grain size are confirmed in the coercivity of these Fe-Si alloy powders. Good magnetic softness, with a saturation magnetization of 198 Am^2/kg and coercivity of ~ 20 A/m, has been achieved. This study validates that mechanical alloying is an effective way to produce single-phase BCC Fe-6.5 wt.% Si alloy powders for applications with magnetic powder cores.

INTRODUCTION

Soft magnetic materials, characterized by high saturation magnetization and small coercivity,[1] have been widely used in power and electronic devices, such as wind turbines, electric vehicles, and power transformers.[2] The materials are required to improve the power density and thus benefit the miniaturization and light weight of these devices.[3] Magnetic core loss determines the energy efficiency of soft magnetic materials. It consists of energy losses due to magnetic hysteresis, macro-eddy currents, and domain wall motion.[4] Impurities, magnetic hard phases, inclusions, grain boundaries, and residual stress can pin the domain wall under a quasi-static field and thus increase the hysteretic loss.[5] An alternating magnetic field introduces eddy currents, both in the macro-scale within skin depth and micro-scale around the domain walls, resulting in Joule heating of the material.[6] The losses increase with the frequency and mainly dissipate in the form of heat. Consequently, the working temperature is elevated, and the magnetic softness of the material deteriorates, especially when the Curie temperature is approached.[7] Fe-6.5 wt.% Si alloys with a BCC structure (A2) are favorable for applications as soft magnetic material, because they have a high saturation magnetic induction of 1.8T,[6,8] a small magnetocrystalline anisotropy of 22 kJ/m^3,[6,9] a near-zero saturation magnetostriction of 0.1 ppm,[6,8] a high electrical resistivity of 82 $\mu\Omega$ cm,[6,10] and a high Curie temperature of 690 °C.[6,11] An iron-based nanocomposite alloy, which consists of α-(Fe,Si) nanograins embedded in an amorphous matrix, was developed in 1988.[12]

Microstructure, Particle Size, and Magnetic Property of Fe-6.5 wt.% Si Nanocrystalline Alloys Prepared by Mechanical Alloying

1067

These alloys are registered as FINEMET with a typical composition of $Fe_{73.5}Si_{13.5}Nb_3B_9Cu_1$, and exhibit ultra-soft magnetic properties.[12]

Fe-6.5 wt.% Si alloys exhibit low power losses at high frequencies and are promising for work at a switch frequency up to 1 MHz,[13] but the α-(Fe,Si) has limited Si solubility (∼ 4.8 wt.%) at room temperature and coexists with other stable phases. Based on the Fe-Si binary phase diagram,[14] ordered phases with B2 and DO3 structures will precipitate out from the BCC solid solution at a high concentration of silicon, and concomitantly introduce antiphase boundaries. These secondary B2-FeSi and DO3-Fe_3Si phases are brittle, which reduces the ductility of the alloy and thus makes it unsuitable for plastic deformation.[15] Also, these antiphase boundaries can pin magnetic domain displacement and thus deteriorate magnetic softness.[16] Ordered phases form inevitably in the Fe-6.5% Si alloy directly solidified from the melt into bulk. Various processing techniques have been used to suppress this ordering transformation occurring either from the liquid or in the solid state, which confines the dimensions of the sample as strips or particles. These techniques include rapid solidification,[13,16–19] thermomechanical processing,[9,20] deposition/diffusion annealing,[13,21] and mechanical alloying,[13,22–24] which rely on ultra-fast cooling rate, extended solid solubility, or severe plastic deformation. Mechanical alloying is a preferred way to produce a single-phase Fe-6.5 wt.% Si alloy with a BCC structure, because of reduced cost and a scalable process.[25] It is feasible to produce nanocrystalline particles[15,22–24] and to control the distribution of particle size.[24,25] In addition, mechanical alloying is a solid-state processing technique and enables the production of non-equilibrium materials,[25] such as supersaturated solid-solution phases with nano-sized grains.[26] During ball milling, repeated fracturing and re-welding of powder particles form a lamellar microstructure, which facilitates the alloying process.[27] Residual strain generated by high-energy ball milling accumulates over the milling time,[15] and couples with magnetostriction to cause an increase of coercivity.[22] These as-milled powders can subsequently be bonded or sintered in bulk to make soft magnetic composites.[28] In this paper, we used a high-energy vibration ball mill to prepare α-(Fe,Si) alloy powders with a Si content of 6.5 wt.% and investigated the structural and magnetic properties of these mechanically alloyed powders.

MATERIALS AND EXPERIMENTAL

Elemental powders of iron (100 mesh, 99.47% pure) and silicon (200 mesh, 99.99% pure) were used as starting materials. The ball mill used was an HF-Kejin MKS-SFM-3. Both milling vials and milling balls were made from 304 stainless steel. The motor of the mill was operated at a fixed speed of 1200 rpm. A ball-to-powder mass ratio of 5:1 was selected for milling. The powder mixtures were ball-milled separately for 0 h, 0.5 h, 1 h, 1.5 h, 3 h, 6 h, 9 h, and 12 h. To avoid excessive heat, the ball mill was stopped every 30 min for 5 min. The as-milled powders were characterized by an X-ray diffractometer (XRD; Dandong Tongda TZL-30Z) with a copper source (Cu Kα, λ = 0.154 nm). The 2θ scans were from 20° to 120° using a step size of 0.02° and a time per step of 0.02 s. The diffraction peaks were deconvoluted by fitting Gaussian functions using Origin® software[29] to obtain a peak location θ, full width at half-maximum β, and integrated intensity. More details about the procedure for XRD peak deconvolution can be found in Ref. 30. The Scherrer equation Eq. 1 was used to estimate the grain size, D, of the powder sample[31] with a calculated error using several diffraction peaks. The lattice parameter was determined by an extrapolation method with the Nelson–Riley function Eq. 2,[32] and an error of 0.005 Å has been assumed.[33] A Williamson–Hall plot Eq. 3 was applied to determine the residual strain, ε, and grain size, D, of the identified phases.[34] The values of grain size determined by both the Scherrer equation and the Williamson–Hall plot were compared to examine the significance of strain-induced peak broadening.[31,32,34]

$$D = 0.9\lambda/(\beta\cos\theta) \tag{1}$$

$$f(\theta) = \frac{1}{2}\left(\frac{\cos^2\theta}{\sin\theta} + \frac{\cos^2\theta}{\theta}\right) \tag{2}$$

$$\beta\cos\theta = 0.9\lambda/D + 4\varepsilon\sin\theta \tag{3}$$

The distribution and cumulative curves of the particle size were characterized by a laser particle size analyzer (Winner 3005). The distribution was fitted by Gaussian functions using Origin® software, and the median diameter (D50) from the cumulative curve was designated as the average particle size. A scanning electron microscope (SEM; ZEISS Sigma 300) equipped with an energy-dispersive X-ray spectrometer (EDS) was used to reveal the morphology and elemental mapping of the samples. Magnetic hysteresis loops were measured by a vibrating sample magnetometer (VSM; Lakeshore 7407) at room temperature with a magnetic field applied up to 20 kA/m. The VSM measurements were conducted in a point-by-point mode, and each sample was tested three times.

RESULTS AND DISCUSSION

Structure

Figure 1 shows the XRD patterns of Fe-6.5% Si alloy powders after milling for 0–12 h. The peaks identified are from α-(Fe,Si) and residual Si phases. Superlattice peaks of ordered phases (B2 and DO3) are not observed in the diffraction patterns, indicating that ordering of the Si atoms does not occur
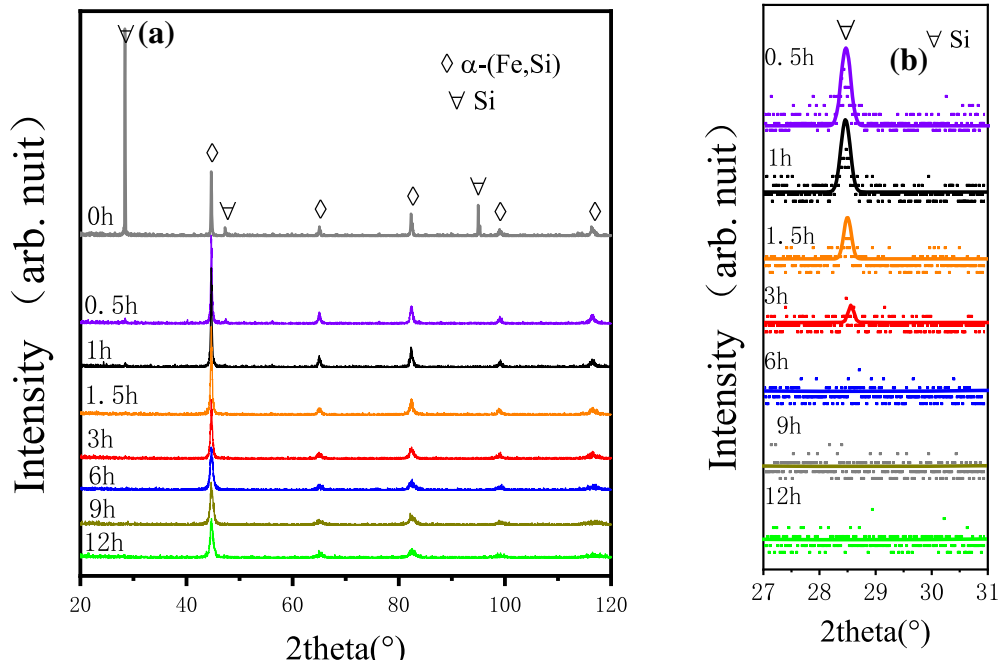
Fig. 1. XRD patterns of Fe-6.5 wt.% Si powders after milling for 0 h, 0.5 h, 1 h, 1.5 h, 3 h, 6 h, 9 h, and 12 h: (a) 2θ from 20° to 120°, (b) a zoom-in plot with 2θ from 27° to 31°; the Y axis is in log scale, data points and fitted curves are shown, and the XRD pattern of 0 h is not included.

and, thus, only the BCC solid-solution phase forms. There are also no diffraction peaks in the XRD patterns for impurities introduced by the grinding medium. The residual Si phase disappears after milling for 3 h (Fig. 1b), and only diffraction peaks of α-(Fe,Si) exist, suggesting the formation of a single α-(Fe,Si) phase. As shown in Fig. 2a, the grain size determined by the Williamson–Hall plot is larger than the values from the Scherrer equation and lies outside the error, suggesting that the lattice strain from ball milling contributes to the peak broadening observed. When the milling time increases, the grain size of the α-(Fe,Si) phase is reduced (Fig. 2a), as exhibited by an obvious peak broadening (Fig. 1a). A small grain size of $\sim$ 10 nm is realized after prolonged milling (> 9 h). During the alloying process, Si atoms dissolve substitution-ally into the α-Fe lattice,[22] causing a decrease in the lattice parameter of the α-(Fe,Si) because the atomic radius of Si is smaller than that of Fe.[35] As shown in Fig. 2b, the lattice parameter of the α-(Fe,Si) decreases significantly at a milling time of 3 h, and then maintains a value of 2.858 ± 0.005 Å, which corresponds to an Si content of $\sim$ 6.6 wt.%.[36] Mechanical alloying of the Fe-Si powder mixtures was completed within a milling time of 3 h, as confirmed both by the disappearance of the Si peaks (Fig. 1b) and the Si content in the α-(Fe,Si) referred from the lattice parameter (Fig. 2b). As shown in Fig. 2c, the strain remaining in the α-(Fe,Si) phase gradually increases as the milling proceeds. The impact energy, accumulated by collisions of the balls during milling, introduces plastic deformation and

residual strain in the powders.[27] After prolonged milling (> 9 h), the residual strain was $\sim$ 0.3%.

Particle Size

Figure 3 shows the distribution of the particle size of alloyed powders at different milling times, and only representative samples (1 h, 3 h, 6 h, and 12 h) are shown. The distributions have multiple modes and are fitted by several Gaussian functions. As the milling time increases, the Gaussian curve of particle size around 10 μm disappears after 3 h (Fig. 3a and b), while the curve around 60 μm exhibits a gradual increase at the expense of a decrease in the curve around 30 μm (Fig. 3b, c and d). The alloyed powders tend to have a homogenous distribution of particle size after prolonged milling. Figure 4 shows cumulative curves and mean values of particle size of these samples. The shape of the cumulative curve (Fig. 4a) correlates with the homogeneity of the particle size and smooth S-shaped curves are observed when the size distribution is nearly a single mode. After milling for 6 h, the average size of the particles is reduced to $\sim$ 30 μm, and only a slight increase is observed as the milling continues (Fig. 4b). It is expected that an equilibrium between fracturing and cold welding is reached, which results in a constant value of average particle size.[15] As shown in Fig. 4b, the particle size decreases when fracturing dominates at intervals of 0–1 h and 3–6 h, while it increases when cold welding dominates at 1–3 h. Alternating the dominant process during the 3 h milling
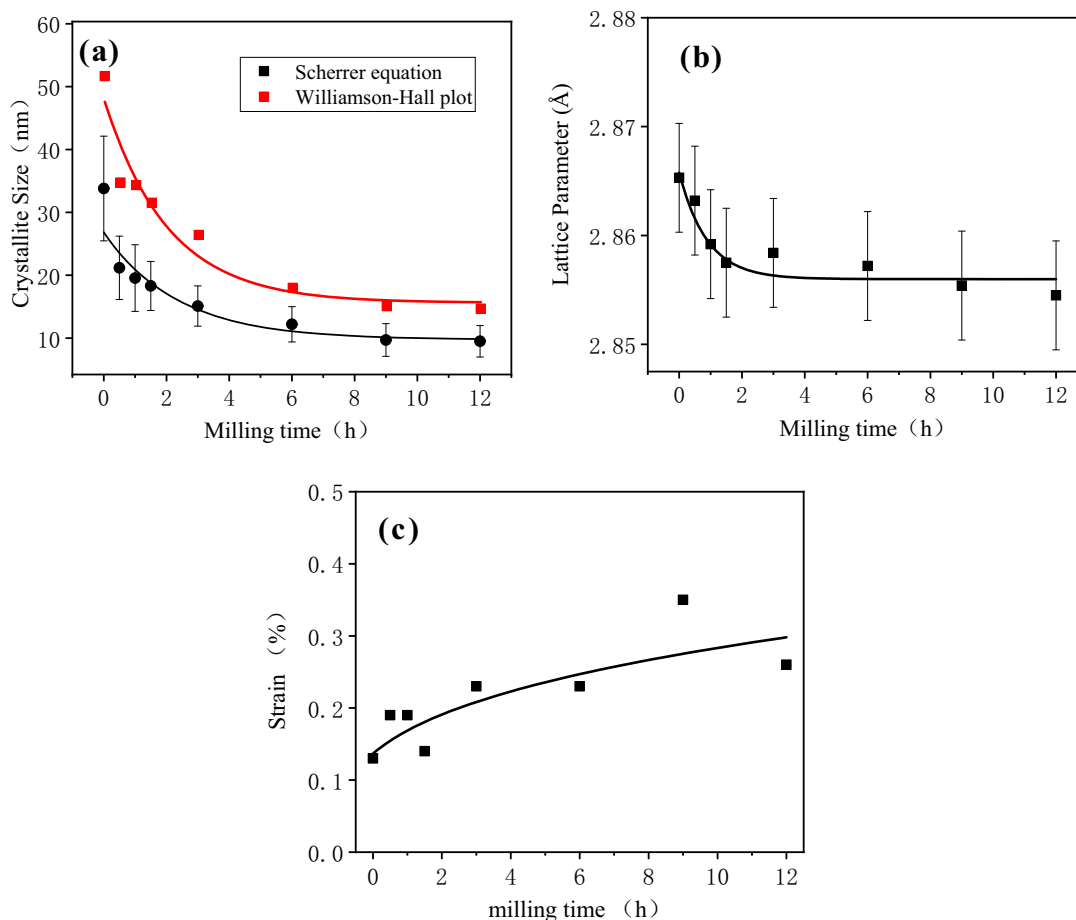
Microstructure, Particle Size, and Magnetic Property of Fe-6.5 wt.% Si Nanocrystalline Alloys
Prepared by Mechanical Alloying

1069

Fig. 2. XRD analyses of Fe-6.5 wt.% Si powders at different milling times: (a) grain size of α-(Fe,Si) determined both from the Scherrer equation and the Nelson–Riley function, (b) lattice parameter of α-(Fe,Si), (c) strain induced in the α-(Fe,Si) phase; the solid curves serve as a guide to the eye.

possibly contributes to the formation of a lamellar microstructure,[25] which facilitates the dissolution of Si atoms into the α-Fe lattice. This alloying process completes after milling for 3 h, as confirmed by the disappearance of the diffraction peaks of Si from the XRD analysis.

Morphology and Elemental Distribution

Figure 5 shows SEM images of the alloyed powders after milling for 1 h, 3 h, 6 h, and 12 h. At the milling time of 1 h (Fig. 5a), small flaky particles (∼ 10 μm) adhere loosely on the surfaces of much larger particles which have an irregular shape and a rough and porous surface. When milled for 3 h, the surfaces of these particles become smooth and dense (Fig. 5b). The particle size is also appreciably enlarged, while the small particles (∼ 10 μm) are rarely visible, which is consistent with the observation of size distribution in Fig. 3b. As the milling proceeds (Fig. 5c and d), the particles tend to become equiaxed. From the SEM images, the particles at 6 h clearly have a smaller size than the ones at 3 h, while the size increases partially for medium-sized particles (∼ 30 μm) at 12 h. This observation agrees with the trend of average particle size shown in Fig. 4b.

Figure 6 shows the EDS mapping of the same samples in Fig. 5. The mapped area is a surface of a selected particle in each powder sample, where the composition consists of Fe, Si, Cr, Mn, and Ni elements, as confirmed by SEM-EDS. The Cr, Mn, and Ni are impurity elements introduced by the milling vial and the milling balls made by 304 stainless steel. Table I lists the contents for all the elements in the sample determined from EDS spectra (not shown), and demonstrates that Fe and Si are the majority elements (> 99 wt.%). Regardless of the milling time, these contamination elements of Cr, Mn, and Ni have uniform elemental distributions. The total content of Cr, Mn, and Ni elements increases slightly with the milling time, but their amount is negligibly small (< 0.8 wt.%) compared to Fe and Si. A significant amount of Si aggregation is observed on the particle surfaces after milling for 1 h and 3 h (Fig. 6a and b, respectively). The Si elements tend to be distributed
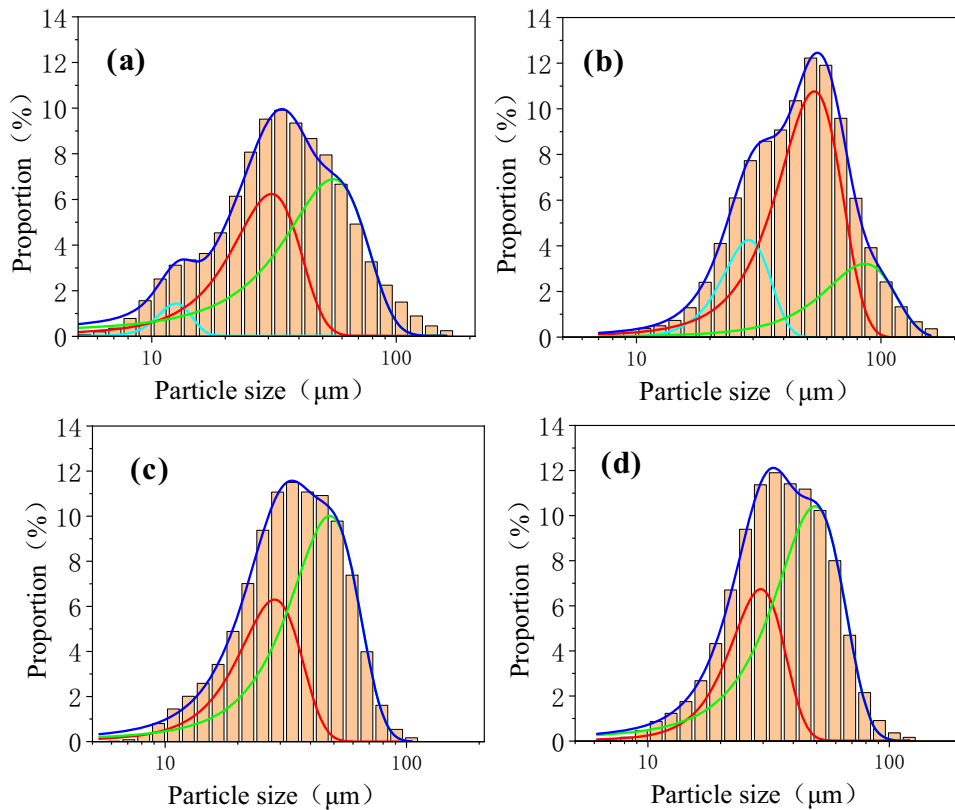
Fig. 3. Particle size distributions of Fe−6. 5wt.% Si powders after milling for (a) 1 h, (b) 3 h, (c) 6 h, and (d) 12 h; Gaussian curves after fitting are shown, and the blue curve is a sum of the fitted curves; the axis of particle size is in a log scale (Color figure online).
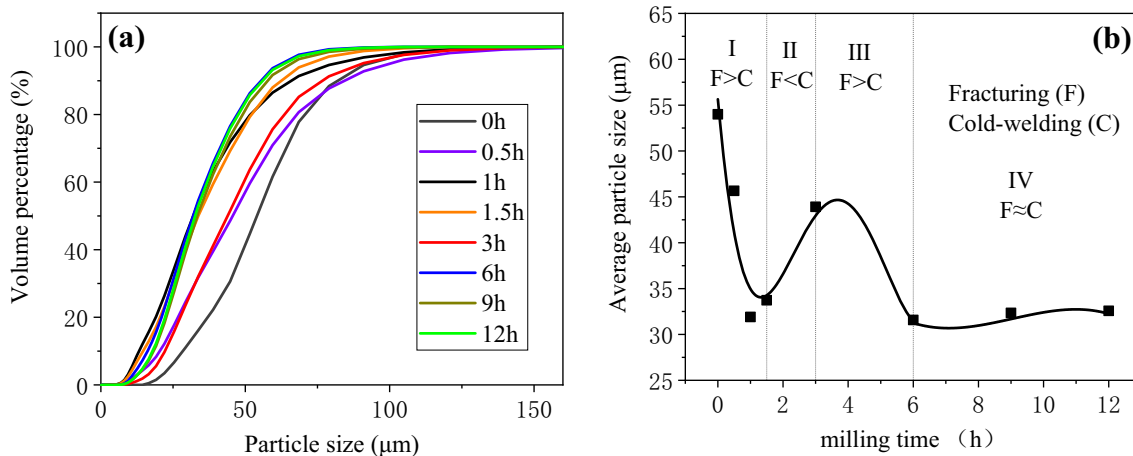

Fig. 4. Analyses of particle size for Fe-6.5 wt.% Si powders at different milling times: (a) cumulative curves of particle size, (b) average particle size (D50) against milling time, which is defined by the value of particle size of the cumulative curve at 50% volume percentage from (a); the solid curves serve as a guide to the eye.

homogeneously as the milling time increases. The elemental distributions of Si match well with Fe at 6 h and 12 h (Fig. 6c and d, respectively), although a few micro-regions ($< 1 \ \mu$m) with Si enrichment exist. This supports the observation of the α-(Fe,Si) solid-solution phase in Fig. 1. Based on the EDS mapping of the Fe and Si elements, the alloying process did not complete after milling for 3 h, which is inconsistent with the XRD result. This

discrepancy lies in the detection limit in the phase amount (5 vol.%) of the conventional XRD technique.[37] One plausible explanation is that, after milling for 3 h, the amount of Si atoms aggregated on the particle surface (Fig. 3b) is less than 5%, while the distributions of the Fe and Si elements inside the particle are homogeneous. The subsequent fracturing, which dominates at the interval between 3 h and 6 h (Fig. 4), blends these Si
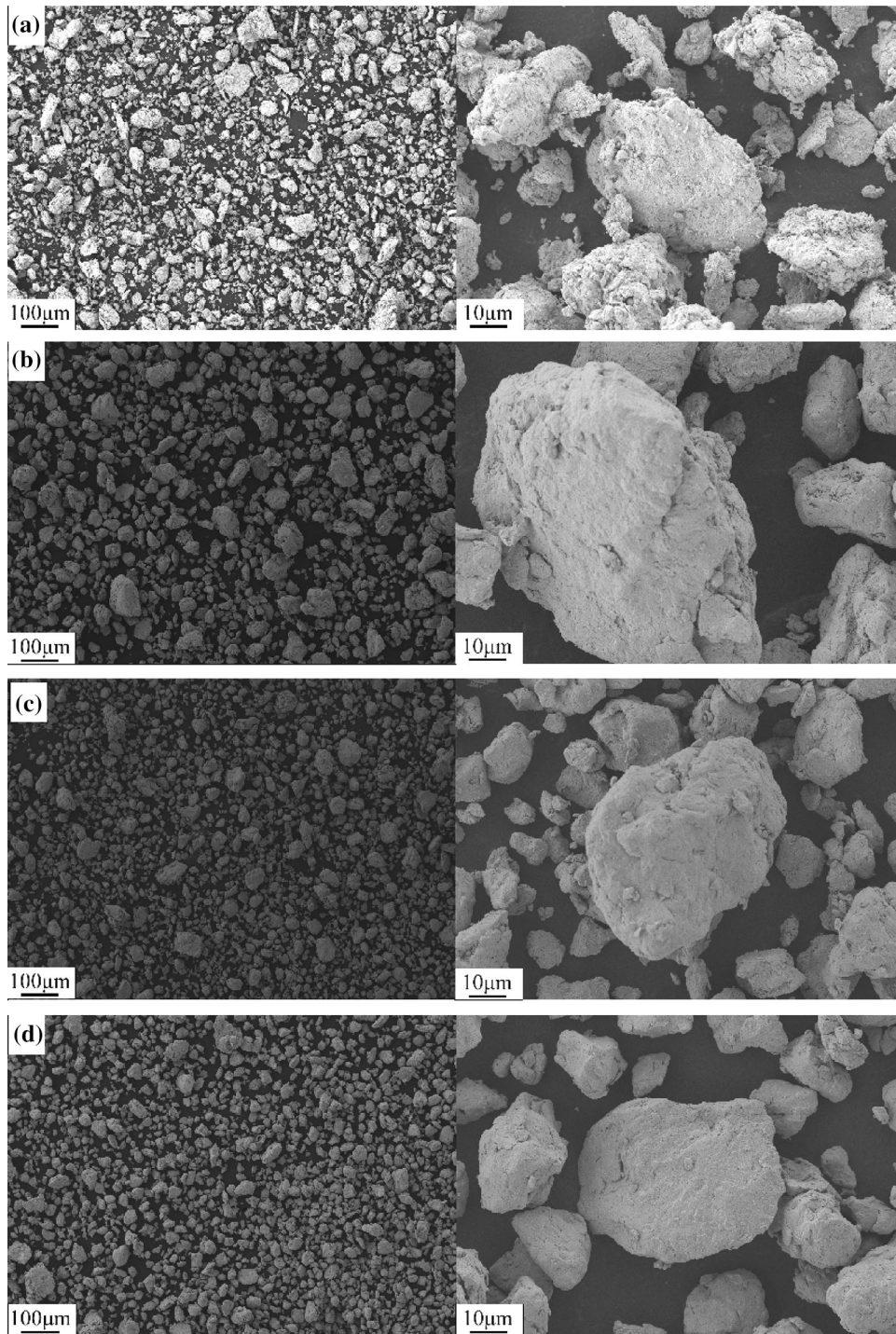
Microstructure, Particle Size, and Magnetic Property of Fe-6.5 wt.% Si Nanocrystalline Alloys
Prepared by Mechanical Alloying

1071

Fig. 5. SEM images (magnified at ×100 and ×1000) of Fe-6.5 wt%Si powders after milling for (a) 1 h, (b) 3 h, (c) 6 h, and (d) 12 h.

aggregates from the surface to the interior of the α-(Fe,Si) particles.

Magnetic Properties

Figure 7 shows hysteresis loops of the powder samples after different milling times. All the samples exhibit ferromagnetic responses to the applied magnetic field. When the milling time increases, the saturation magnetization of the samples drops rapidly at first (< 3 h) and then decreases slowly (> 3 h), as demonstrated in Fig. 8a. The rate of magnetization change correlates with the solid-state transformations occurring. The rapid drop in magnetization is caused by mechanical alloying to form the α-(Fe,Si) phase. Non-magnetic Si atoms dissolve substitutionally into the α-Fe lattice, which reduces the number of ferromagnetic Fe atoms in
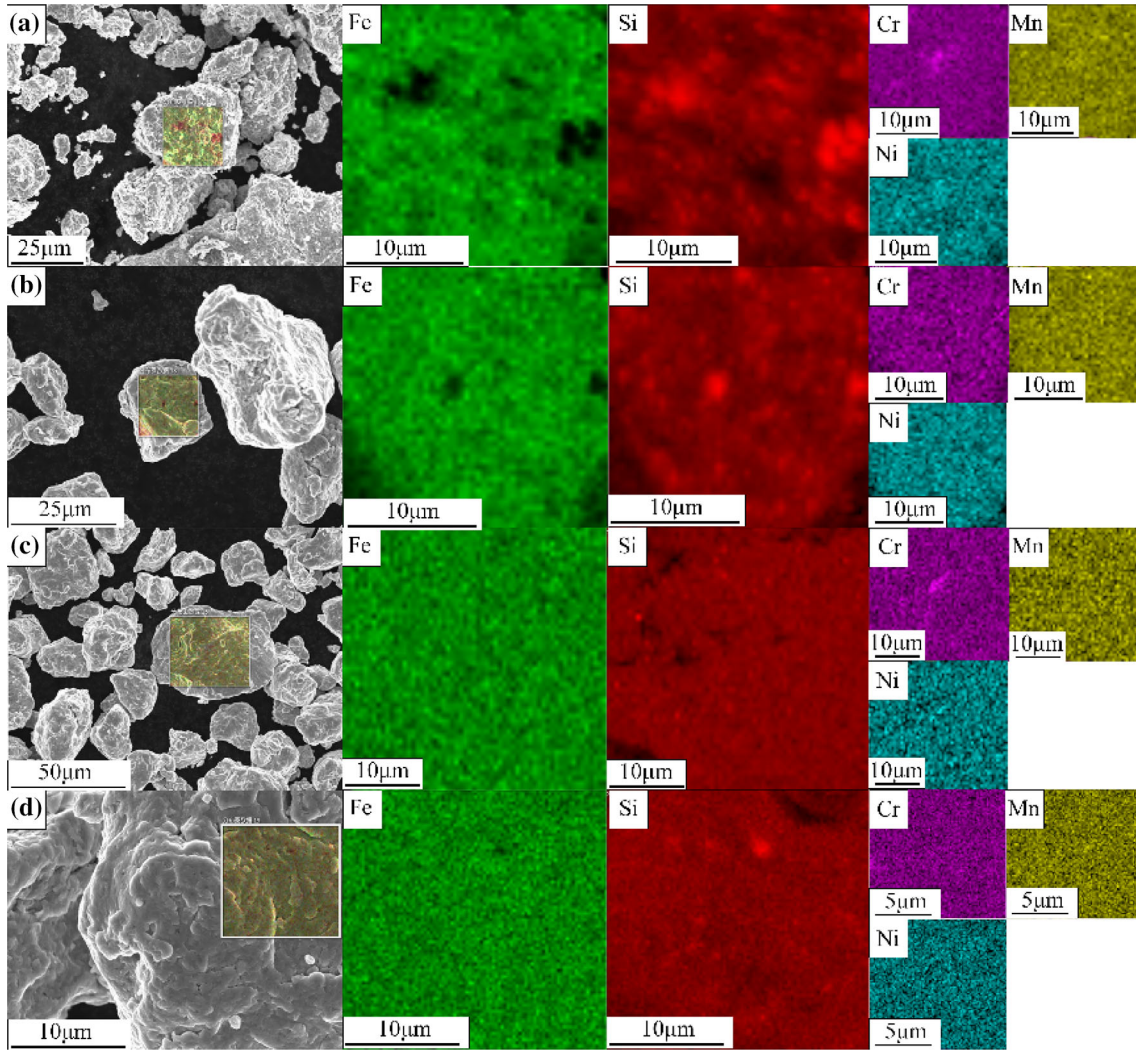
Fig. 6. EDS mapping of Fe-6.5 wt%Si powders after milling for (a) 1 h, (b) 3 h, (c) 6 h, and (d) 12 h; Fe and Si are the majority elements while Cr, Mn and Ni are the minority elements; the mapped areas are indicated in the SEM images.

Table I. Elemental contents of Fe-6.5 wt.% Si powders after milling for 1 h, 3 h, 6 h, and 12 h from SEM-EDS analyses

As-milled sample (h)	Elemental contents (wt.%)				
	Fe	Si	Cr	Mn	Ni
1	91.65	7.83	0.18	0.22	0.12
3	93.29	6.06	0.28	0.17	0.13
6	92.63	6.73	0.39	0.13	0.13
12	93.08	6.22	0.38	0.24	0.18

the nearest neighbor, resulting in magnetic dilution.[25] The slow decrease in magnetization is attributed to non-magnetic contamination gradually accumulating with the milling time,[15] which is inevitable for the process of ball milling.

The coercivity of the samples shows a peak when plotted against the milling time (Fig. 8b), and their

values are much smaller than 100 A/m. Based on a random anisotropy model,[8,38] the coercivity of the nanocrystalline alloys is proportional to the sixth power of grain size (D^6), where magnetocrystalline anisotropy (K_1) dominates. An abnormal increase in coercivity from 0 h to 1.5 h is observed while the grain size is reduced from ~ 35 nm to ~ 15 nm. An increase of Si content in the α-(Fe,Si) phase cause a dramatical decrease in K_1, while the saturation magnetostriction coefficient, λ_s, remains at ~ 20 ppm up to 4.5 wt.% Si (Fig. 9a).[6] Given that the residual strain (or the stress σ) increases with the milling time (Fig. 2c), the magnetoelastic anisotropy, $K_\sigma = 3/2 \, \sigma \, \lambda_s$,[8] increases accordingly. The K_σ could be larger than K_1 and dominate the coercivity.[39] As a result, the coercivity increases abnormally with reduced grain sizes from 0 h to 3 h due to magnetoelastic anisotropy. As demonstrated previously, the alloying process completes at the milling time of 3 h, and ~ 6.5 wt.%Si dissolves in the α-(Fe,Si). A near-zero λ_s (0.6 ppm) is reached

Microstructure, Particle Size, and Magnetic Property of Fe-6.5 wt.% Si Nanocrystalline Alloys
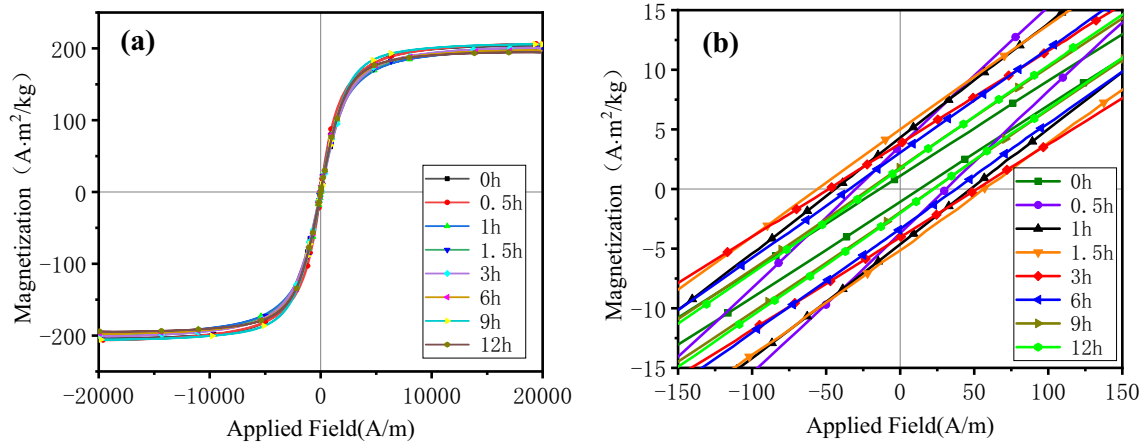Prepared by Mechanical Alloying

1073

Fig. 7. VSM measurement of Fe-6.5 wt% Si powders at different milling times: (a) magnetic hysteresis loops under a maximum field of 20 kA/m, (b) a zoom-in plot of (a) near the origin; the solid curves serve as a guide to the eye.
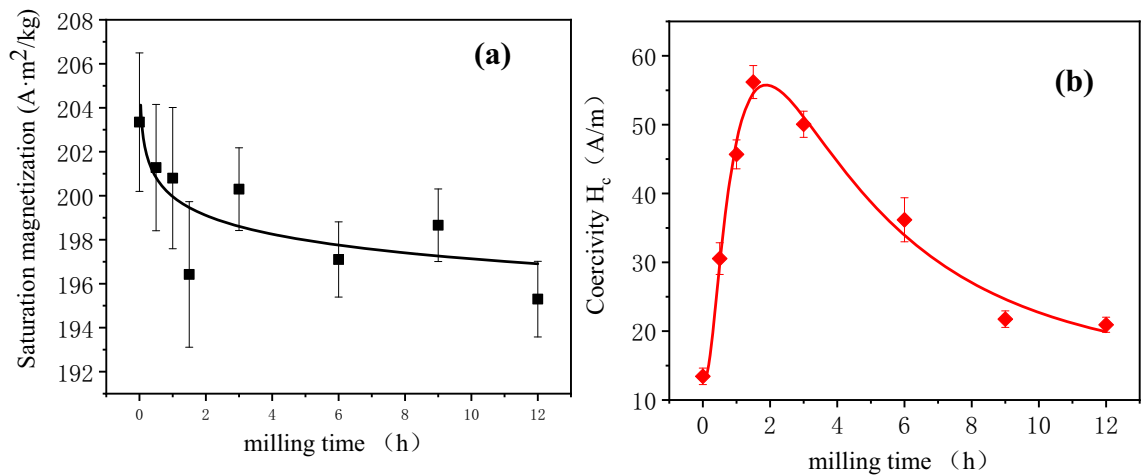

Fig. 8. Magnetic properties of Fe-6.5 wt% Si alloy powders against milling time: (a) saturation magnetization, (b) coercivity; the solid curves serve as a guide to the eye.
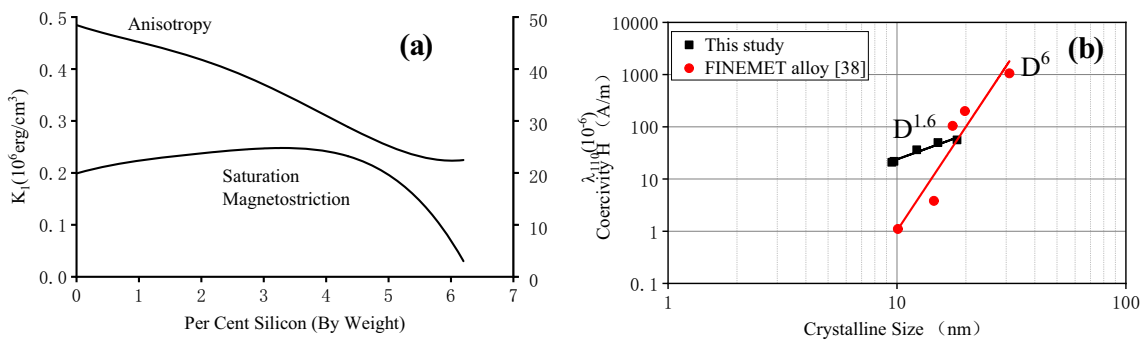

Fig. 9. (a) Compositional dependence of magnetocrystalline anisotropy coefficient, K_1, and saturation magnetostriction coefficient, λ_s, in α-(Fe,Si) alloys; reprinted with permission from Ref. 6. (b) Coercivity of Fe-6.5 wt.% Si alloy powders against grain size (in black); the axes are in log scale. Data of a FINEMET nanocrystalline alloy (Fe$_{73.5}$Si$_{13.5}$Nb$_3$B$_9$Cu$_1$)[38] are included for comparison (in red) (Color figure online).

and the K_1 becomes larger than the K_σ. Therefore, a decrease in coercivity occurs from 3 h to 12 h (Fig. 7b), which is consistent with the slight decrease in the grain size (Fig. 2a). The dependence of coercivity on grain size for alloyed powders, as demonstrated in Fig. 9b, is about 1.6 power ($D^{1.6}$). This deviation from the sixth power law (D^6) possibly results from the remaining magnetoelastic anisotropy[22,39] or the distribution of grain size.[22,38]

CONCLUSION

Mechanical alloying of Fe and Si powders successfully produces a single α-(Fe,Si) solid-solution phase with a high Si content of 6.5 wt.%. The reaction that forms the α-(Fe,Si) phase completes after 3 h milling, as confirmed by the XRD pattern and the elemental mapping. Both the lattice constant and the grain size of the α-(Fe,Si) first decline as the milling time increases, and then maintain constant values of 2.858 Å and ~ 10 nm, respectively. After a prolonged milling ($>$ 6 h), an equilibrium between fracturing and cold welding is reached. Therefore, powders having an equiaxed morphology, a small particle size (~ 30 μm), and a uniform size distribution are obtained. The alloying process decreases the saturation magnetization of the alloy powders, mainly because of the substitutional dissolution of non-magnetic Si atoms into the α-Fe lattice. An abnormal increase in coercivity is also observed while the grain size is reduced, resulting from magnetoelastic anisotropy with an induced strain up to 0.3%. When the alloying is completed, coercivity decreases to 1.6 power of the grain size. The alloyed powders at milling time of 9 h and 12 h exhibit good magnetic softness with a saturation magnetization of ~ 198 A m^2/kg and a coercivity of ~ 20 A/m. This study confirms that mechanical alloying can produce single-phase BCC Fe-6.5 wt.% Si alloy powders as soft magnetic materials.

ACKNOWLEDGEMENT

CONFLICT OF INTEREST

On behalf of all authors, the corresponding author states that there is no conflict of interest.

REFERENCES

1. A. Krings, A. Boglietti, A. Cavagnino, and S. Sprague, *IEEE Trans. Ind. Elctron.* 64, 2405 https://doi.org/10.1109/TIE.2016.2613844 (2017).
2. J.M. Silveyra, E. Ferrara, D.L. Huber, and T.C. Monson, *Science* 362, 6413 https://doi.org/10.1126/science.aao0195 (2018).
3. O. Gutfleisch, M.A. Willard, E. Brück, C.H. Chen, S.G. Sankar, and J.P. Liu, *Adv. Mater.* 23, 821 https://doi.org/10.1002/adma.201002180 (2011).
4. A.S. Inoue and N. Nishiyama, *MRS Bull.* 32, 651 https://doi.org/10.1557/MRS2007.128 (2007).
5. O.A. Tretiakov, D.R. Clarke, G. Chern, Y.B. Bazaliy, and O. Tchernyshyov, *Phys. Rev. Lett.* 100, 127204 https://doi.org/10.1103/PhysRevLett.100.127204 (2008).
6. R.C. Ohandley, *Modern Magnetic Materials: Principles and Applications* (Wiley, New York, 2000), pp338–347.
7. M.A. Willard, M. Daniil, and K.E. Kniping, *Scr. Mater.* 67, 554 https://doi.org/10.1016/J.SCRIPTAMAT.2011.12.043 (2012).
8. G.D. Herzer, *Acta Mater.* 61, 718 https://doi.org/10.1016/j.actamat.2012.10.040 (2013).
9. H. Fu, Y. Mo, Z. Zhang, and J. Xie, *Mater. Sci. Eng.* 656, 90 https://doi.org/10.1016/J.MSEA.2016.01.036 (2016).
10. M.F. Littmann, *IEEE Trans. Magn.* 7, 48 https://doi.org/10.1109/TMAG.1971.1066998 (1971).
11. W.J. Yuan, R. Li, Q. Shen, and L. Zhang, *Mater Charact* 58, 376 https://doi.org/10.1016/J.MATCHAR.2006.06.003 (2007).
12. Y. Yoshizawa, S. Oguma, and K. Yamauchi, *J. Appl. Phys.* 64, 6044 https://doi.org/10.1063/1.342149 (1988).
13. G. Ouyang, X. Chen, Y. Liang, C.R. Macziewski, and J. Cui, *J. Magn. Magn. Mater.* 481, 234 https://doi.org/10.1016/J.JMMM.2019.02.089 (2019).
14. P.R. Swann, L. Granas, and B. Lehtinen, *Metal Sci.* 9, 90 https://doi.org/10.1179/030634575790445279 (1975).
15. Z. Bensebaa, B. Bouzabata, and A. Otmani, *J. Alloys Compd.* 469, 24 https://doi.org/10.1016/J.JALLCOM.2008.01.151 (2009).
16. C.C. Lima, M.C.A. da Silva, M.D.C. Sobral, R.E. Coelho, and C. Bolfarini, *J. Alloys Compd.* 586, S314 https://doi.org/10.1016/J.JALLCOM.2012.09.074 (2014).
17. P. Arató, I. Bóc, and T. Gróf, *J. Magn. Magn. Mater.* 41, 53 https://doi.org/10.1016/0304-8853(84)90135-5 (1984).
18. B. Viala, J. Degauque, M. Fagot, M. Baricco, E. Ferrara, and F. Fiorillo, *Mater. Sci. Eng. A* 212, 62 https://doi.org/10.1016/0921-5093(96)10188-X (1996).
19. S. Cui, G. Ouyang, T. Ma, C.R. Macziewski, V.I. Levitas, L. Zhou, M.J. Kramer, and J. Cui, *J. Alloys Compd.* 771, 643 https://doi.org/10.1016/J.JALLCOM.2018.08.293 (2019).
20. J.S. Shin, J.S. Bae, H.J. Kim, H.M. Lee, T.D. Lee, E.J. Lavernia, and Z.H. Lee, *Mater. Sci. Eng. A* 407, 282 https://doi.org/10.1016/J.MSEA.2005.07.012 (2005).
21. H. Yu, W. Yu, and X. Bi, *J. Alloys Compd.* 634, 83 https://doi.org/10.1016/J.JALLCOM.2015.01.156 (2015).
22. M. Li, R. Birringer, W.L. Johnson, and R.D. Shull, *Nanostruct. Mater.* 3, 407 https://doi.org/10.1016/0965-9773(93)90106-L (1993).
23. C. Stanciu, F. Popa, I. Chicinas, and O. Isnard, *Adv Electron Forum.* 13, 109 https://doi.org/10.4028/www.scientific.net/AEF.13.109 (2015).
24. T. Clark and S.N. Mathaudhu, *J. Magn. Magn. Mater.* 484, 350 https://doi.org/10.1016/J.JMMM.2019.03.070 (2019).
25. C. Suryanarayana, *Prog. Mater. Sci.* 46, 1 https://doi.org/10.1016/S0079-6425(99)00010-9 (2001).
26. W. Shen, F. Wang, D. Boroyevich, and C.W. Tipton, *IEEE Trans. Power Electron.* 23, 475 https://doi.org/10.1109/TPEL.2007.911881 (2007).
27. M. Abdellaoui, T. Barradi, and E. Gaffet, *J. Alloys Compd.* 198, 155 https://doi.org/10.1016/0925-8388(93)90159-K (1993).
28. H. Shokrollahi and K. Janghorban, *J. Mater. Process. Technol.* 189, 1 https://doi.org/10.1016/j.jmatprotec.2007.02.034 (2007).
29. Origin®. https://www.origin.com/hkg/en-us/. Accessed June 9th 2023.
30. C. Groschner, S. Lan, A. Wiase, A. Leary, M.S. Lucas, C. Park, D.E. Laughlin, M. Diaz-Michelena, and M.E. McHenry, *IEEE Trans. Magn.* 49, 4273 https://doi.org/10.1109/TMAG.2013.2250928 (2013).
31. U. Holzwarth and N. Gibson, *Nat. Nanotechnol.* 6, 534 https://doi.org/10.1038/nnano.2011.145 (2011).
32. J.B. Nelson and D.P. Riley, *Proc. Phys. Soc.* 57, 160 https://doi.org/10.1088/0959-5309/57/3/302 (1945).
33. J.B. Nelson and D.P. Riley, *Proc. Phys. Soc.* 57, 477 https://doi.org/10.1088/0959-5309/57/6/303 (1945).
34. G.K. Williamson and W.H. Hall, *Acta Metall.* 1, 22 https://doi.org/10.1016/0001-6160(53)90006-6 (1953).
35. F. González and Y. Houbaert, *Rev. Metal.* 49, 178 https://doi.org/10.3989/revmetalm.1223 (2013).
36. R.M. Bozorth, *Ferromagnetism* (D. Van Nostrand, New Jersey, 1951), pp74–75.
37. B.D. Cullity, *Elements of X-Ray Diffraction* (Addison-Wesley, Massachusetts, 1956), p395.
38. G.D. Herzer, *IEEE Trans. Magn.* 26, 1397 https://doi.org/10.1109/20.104389 (1990).

39. B. Dong, J. Healy, S. Lan, M. Daniil, and M.A. Willard, *AIP Adv.* 8, 056124 https://doi.org/10.1063/1.5007248 (2018).

Publisher's Note Springer Nature remains neutral with regard to jurisdictional claims in published maps and institutional affiliations.